

Cite this: *J. Mater. Chem. A*, 2021, 9, 607

Activity of layered swedenborgite structured $\text{Y}_{0.8}\text{Er}_{0.2}\text{BaCo}_{3.2}\text{Ga}_{0.8}\text{O}_{7+\delta}$ for oxygen electrode reactions in at intermediate temperature reversible ceramic cells†

Ji-Seop Shin,^a Hyunyoung Park,^a Kwangho Park,^a Muhammad Saqib,^a Minkyong Jo,^a Jung Hyun Kim,^b Hyung-Tae Lim,^c Minseuk Kim,^a Jongsoon Kim^a and Jun-Young Park^{*a}

To improve the thermal stability and intrinsically sluggish kinetics of oxygen electrode reactions in solid oxide fuel cells (SOFCs) and reversible protonic ceramic cells (RPCCs) at intermediate temperatures, a novel layered swedenborgite structure $\text{Y}_{0.8}\text{Er}_{0.2}\text{BaCo}_{3.2}\text{Ga}_{0.8}\text{O}_{7+\delta}$ (YEBCG) catalyst is introduced as an alternative to perovskite materials that contain cobalt. The thermal expansion coefficient of YEBCG is $8.41 \times 10^{-6} \text{ K}^{-1}$, which is relatively well matched to the state-of-the-art proton-conducting and oxygen-ion-conducting electrolytes. The chemical bulk diffusion and surface exchange coefficients of YEBCG are 7.12×10^{-4} and $8.01 \times 10^{-3} \text{ cm}^2 \text{ s}^{-1}$, respectively, at 650 °C, which leads to much faster action than with state-of-art perovskite structured materials at intermediate temperatures. The maximum power densities of YEBCG cells are notably high, reaching 0.77 and 0.83 W cm^{-2} at 650 °C in SOFC and protonic ceramic fuel cell modes, respectively. Under electrolysis, the YEBCG cells achieve outstanding current densities of -0.61 and -4.42 A cm^{-2} at 500 and 700 °C, respectively, under an applied voltage of 1.4 V. Furthermore, the RPCC with YEBCG present no degradation over an entire 1000 h in fuel cell and electrolysis cell modes. These results demonstrate the excellent properties, including good durability, of the YEBCG air electrode when used in high performance SOFCs and RPCCs.

Received 11th November 2020
Accepted 3rd December 2020

DOI: 10.1039/d0ta11000k

rsc.li/materials-a

Introduction

Solid oxide fuel cells (SOFCs) are well regarded as sustainable and efficient electrochemical energy conversion devices because of their high energy conversion efficiency, excellent fuel flexibility, and low environmental impact. However, conventional SOFCs operate at high temperatures (>700 °C), this leads to high costs due to constraints on material selection and limited long-term thermal stability.^{1–3} To overcome these limitations at high operating temperatures, many researchers have investigated reducing the operating temperatures of SOFCs to intermediate temperatures (IT, 500–700 °C) through the use of high ionic conductivity ceria-based electrolytes (e.g. $\text{Sm}_{0.2}\text{Ce}_{1.8}\text{O}_{2-\delta}$) that work well at reduced temperatures.^{4,5} Recently, protonic ceramic fuel cells (PCFCs), which show low activation energies

(0.3–0.6 eV) for proton transport at reduced temperatures (<700 °C), have received a tremendous amount of interest as an alternative to high temperature SOFCs. PCFCs have various advantages, they alleviate problems in areas such as material compatibility for cell fabrication and long-term thermal stress durability as well as having a higher CH_4 conversion ratio and better carbon coking resistance with hydrocarbon fuels compared to SOFCs.^{6–8}

More recently, the PCFC technology has been extended to include reversible protonic ceramic cells (RPCCs) that address some energy storage and conversion challenges.⁹ RPCCs, which can operate in protonic ceramic fuel cell (PCFC) mode and electrolysis cell (PCEC) mode as a single electrochemical device, supply versatile pathways for energy storage and conversion of the inherently intermittent electricity produced from renewable energy sources.^{10–12} However, the electrochemical performance of IT-SOFCs and RPCCs stills needs to be improved in terms of electrical performance and reliability at low-to-intermediate temperatures in order to make their use commercially feasible. In particular, research into materials with high intrinsic oxygen reduction (ORR) and evolution reaction (OER) activity for use in IT-SOFCs and RPCCs is still lacking, especially at low-to-intermediate temperatures. This is despite the fact

^aHMC, Department of Nanotechnology and Advanced Materials Engineering, Sejong University, Seoul 05006, Korea. E-mail: jyoung@sejong.ac.kr; Tel: +82 2 3408 3848

^bDepartment of Advanced Materials Science and Engineering, Hanbat National University, Daejeon 34158, Korea

^cSchool of Materials Science and Engineering, Changwon National University, Changwon 51140, Korea

† Electronic supplementary information (ESI) available. See DOI: 10.1039/d0ta11000k

that the poor polarization resistance (R_p) of ceramic cells primarily originates from the sluggish kinetics of the air electrode materials being used.^{13–15}

Of late, several novel approaches have been proposed to enhance the simultaneous migration of protons, oxygen-ions, and electrons through morphological tuning (e.g., infiltration and exsolution) of the proton-conducting mixed ionic–electronic (MIE) conducting composites at reduced temperatures.^{16,17} However, research into highly electrocatalytic active air electrode materials for ORR/OER is even more crucial at this time because there is still possibility for further performance enhancement through morphological tuning once the optimum materials are identified. Until now, Co-containing single and double perovskite materials, such as $\text{Ba}_{0.5}\text{Sr}_{0.5}\text{Co}_{0.8}\text{Fe}_{0.2}\text{O}_{3-\delta}$ (BSCF), $\text{PrBa}_{0.5}\text{Sr}_{0.5}\text{Co}_{1.5}\text{Fe}_{0.5}\text{O}_{5+\delta}$ (PBSCF), and $\text{NdBa}_{0.5}\text{Sr}_{0.5}\text{Co}_{1.5}\text{Fe}_{0.5}\text{O}_{5+\delta}$ (NBSCF) have been used as the air electrode materials for RPCCs because of their excellent ORR/OER activity with high mixed ionic and electronic conductivity at intermediate temperatures.^{18–20} In addition, recent studies have demonstrated substantial water uptake and proton transport in double perovskite cobaltite systems.^{21,22} This property allows the simultaneous migration of protons, oxygen-ions, and electrons, resulting in high-performance RPCCs at intermediate temperatures. This is because water generation and dissociation reactions take place with ORR and OER, respectively. However, the thermal behavior of most cobaltite materials differs considerably from that of state-of-the-art proton-conducting and oxygen-ion conducting electrolytes [e.g. $\text{BaCe}_{0.7}\text{Zr}_{0.1}\text{Y}_{0.1}\text{Yb}_{0.1}\text{O}_{3-\delta}$ (BCZYYb), $\text{BaZr}_{0.85}\text{Y}_{0.15}\text{O}_{3-\delta}$, $\text{Gd}_{0.1}\text{Ce}_{0.8}\text{O}_{2-\delta}$, and $\text{Sm}_{0.1}\text{Ce}_{0.8}\text{O}_{2-\delta}$ (SDC)]. For example, the thermal expansion coefficient (TEC) value of BCZYYb electrolyte is $9.5 \times 10^{-6} \text{ K}^{-1}$, while BSCF, NBSCF, and PBSCF show extraordinary high TEC values of 23.2×10^{-6} , 24.7×10^{-6} , and $23.7 \times 10^{-6} \text{ K}^{-1}$, respectively.^{23–25} The high TECs of Co-based perovskites are related to the Co^{3+} cation state in those materials, this can transit from low spin ($t_{2g}^5e_g^0$), to intermediate ($t_{2g}^5e_g^1$), to high spin ($t_{2g}^4e_g^2$) progressively, increasing its ionic radius at high temperature.²⁶ This indicates that Co-containing perovskites could possibly be more detrimental in terms of long-term thermal stability because of the mismatch in TEC can impose severe mechanical stress between cell components.²⁷

Co-containing swedenborgite structured $\text{YBaCo}_4\text{O}_{7+\delta}$ (YBC) materials are promising oxygen electrodes for IT-SOFCs and RPCCs on account of their very low TECs ($8\text{--}11 \times 10^{-6} \text{ K}^{-1}$), which are very close to that of the BCZYYb electrolyte.^{28,29} The crystal structure of YBC consists of layers formed by two different types of CoO_4 tetrahedral, $(\text{Co}1)\text{O}_4$ and $(\text{Co}2)\text{O}_4$, which are characterized by different bond lengths with a 1 : 3 ratio.³⁰ Hence, the YBC materials maintain high-spin states in a wide temperature range (no spin transition in Co^{2+} and Co^{3+} at high temperature). Furthermore, an acceptable level of MIC conductivity, a significantly large oxygen-storage capacity (2600 $\mu\text{mol O per g}$), and structural similarity to other cobaltites, provide good prospects for their use as air electrode materials in PCFCs.^{31–33} However, the YBC materials undergo severe phase decomposition at 600–800 °C due to the preference of Co cations for octahedral coordination, which makes their

application in IT-SOFCs and RPCCs difficult.³⁴ More recently, Manthiram *et al.*³⁵ reported that YBC is completely stabilized by partial substitution of Ga in Co sites at 600–800 °C. Danilov *et al.*³⁶ also demonstrated that other dopants, such as Fe and Zn, in the Co sites improved the catalytic activity toward ORRs in SOFCs. However, a comprehensive study of the doping effects on electrochemical performances and phase stability in YBC-based swedenborgite oxides for SOFCs and RPCCs at intermediate temperature has yet to be carried out.

Herein, a systematic examination to gain fundamental understanding is carried out with a goal to improve the ORR/OER catalytic activity and phase stability of YBC-based swedenborgite oxides used in SOFCs and RPCCs as the air electrode material. We selected various doping elements, including lanthanides (Nd, Ce, La, Gd, Er, and Sm) and (post-) transition metals (Co, Cu, Mn, Ni, Fe, Ga, Cr, Al, and Ti) for Y- and Co-sites, respectively, for the YBC-based materials. The doping effect on the electrical properties of the YBC is investigated as functions of the dopants and their composition in a symmetrical cell. The electrochemical impedance spectroscopy (EIS) results identified that $\text{Y}_{0.8}\text{Er}_{0.2}\text{BaCo}_{3.2}\text{Ga}_{0.8}\text{O}_{7+\delta}$ (YEBCG) exhibits much lower area specific resistances (ASRs) in comparison to YBC. The maximum power densities of the YEBCG cell are outstandingly high, reaching 1.30 and 1.35 W cm^{-2} at 700 °C, respectively, in SOFC and PCFC mode. The YEBCG RPCC achieved remarkably high current densities of -0.61 A cm^{-2} at 500 °C at an applied voltage of 1.4 V and the faradaic efficiency of 97.2% at an applied current of 0.5 A cm^{-2} demonstrating that the YEBCG cell produces the theoretically expected amount of H_2 . In addition, the YEBCG cell presented no degradation during the entire 400 h operation in PCFC mode and 500 h in electrolysis cell mode at 600 °C.

Experimental

Synthesis and characterization of swedenborgite structured YBC materials

YBC-based oxides were synthesized using a solid-state reaction method with proper stoichiometric amounts of precursors; BaCO_3 , Y_2O_3 , CeO_2 , Nd_2O_3 , La_2O_3 , Co_3O_4 , CuO , MnO_2 , NiO , Fe_2O_3 (99–99.9% purity, Alfa Aesar), Ga_2O_3 , CrO_3 , Al_2O_3 , TiO_2 (99.9% purity, Sigma Aldrich), Gd_2O_3 , Er_2O_3 , Yb_2O_3 , and Sm_2O_3 (99.9% purity, LTS Chem). The metal oxides were ball-milled using zirconia balls at the appropriate stoichiometric ratio in ethanol for 24 h and then dried at 60 °C in oven overnight. The as-prepared $\text{Y}_{1-x}\text{Ln}_x\text{BaCo}_4\text{O}_{7+\delta}$ ($\text{Ln} = \text{La}, \text{Nd}, \text{Ce}, \text{Gd}, \text{Sm}, \text{Er},$ and Yb) and $\text{YBaCo}_{4-x}\text{Tr}_x\text{O}_{7+\delta}$ ($\text{Tr} = \text{Fe}, \text{Ga}, \text{Ni}, \text{Mn}, \text{Cu}, \text{Cr}, \text{Al},$ and Ti) precursors were calcined at 1100 °C for 6 h to obtain single swedenborgite structured materials. The Er and Ga-doped YBC ($\text{Y}_{0.8}\text{Er}_{0.2}\text{BaCo}_{3.2}\text{Ga}_{0.8}\text{O}_{7+\delta}$, YEBCG) was calcined at 1200 °C for 12 h in air. After calcination, the powders were pulverized using a mortar and pestle to give a uniform particle size.

To investigate the crystalline structure of materials, the X-ray diffraction (XRD, X'Pert, PAN analytical) technique was used with a step size of 0.026° in a 2θ range of 20°–80° under Cu-K α radiation. The diffraction peaks of the miller index were utilized

to obtain the lattice parameters of the swedenborgite structured materials from hexagonal interplanar distances. XRD Rietveld structural refinement was also carried out using FullProf software. In addition, XRD was performed to characterize potential phase reactions between cell components during high-temperature sintering/calcination. The morphology and microstructure of the cell components were characterized by the use of field emission scanning electron microscopy (FESEM, SU-8010, Hitachi) and high resolution transmission electron microscopy (HRTEM, JEM 2100F, JEOL, 200 kV) with energy-dispersive X-ray spectroscopy (EDX, HORIBA). The compositions and chemical bonding states of the YBC were determined using a K-Alpha Plus X-ray photoelectron spectrometer (XPS, Thermo Scientific) with an Al K α X-ray source of $h\nu = 1486.6$ eV. The thermal expansion coefficient (TEC) values of YBC and YEBCG were acquired using a dilatometer (L75H, LINSEIS) from room temperature to 900 °C with a heating/cooling rate of 5 °C min⁻¹ in air. For the TEC measurements, the YBC and YEBCG powders were uniaxially pressed to fabricate a 4.1 × 4.1 × 22 mm rectangular bar that was then sintered at 1250 °C (for YBC) or 1300 °C (for YEBCG) for 24 h in air.

Fabrications of symmetric and anode-supported cells

In order to measure the ASR for all YBC samples including the doped YBC, symmetric cells based on Sm_{0.2}Ce_{0.8}O_{2- δ} (SDC) electrolytes were prepared. The SDC powders (produced by Kceracell, Korea) were uniaxially pressed under 18 MPa for 1 min in a circular mold then sintered at 1650 °C for 10 h in air to acquire very dense electrolyte pellets. Electrode inks were prepared by mixing YBC-based materials with ESL 441 vehicle (ESL ElectroScience), these were then screen-printed on both sides of the electrolyte pellet and sintered at 950 °C for 2 h.

The NiO-SDC and NiO-BCZYYb (65 : 35 wt%) anode-supported cells were fabricated using the tape-casting method. The NiO (Kceracell) and SDC (and BCZYYb, Kceracell) powders were ball-milled with poly methyl methacrylate (Alfa Aesar), fish oil (Aldrich), polyvinyl butyral (Butvar), di-*n*-butyl phthalate (Daejung Chemicals), and polyethylene glycol (Acros) in toluene (Aldrich) and ethyl alcohol solutions for 48 h. The NiO-SDC (and BCZYYb) slurries were cast into a polyester mylar film using a doctor blade system (Hansung Systems) before being pre-sintered at 900 °C for 2 h. The anode functional layer (AFL) and electrolyte slurries were mixed with polyvinyl butyral, di-*n*-butyl phthalate, and Solsperse (SG24000, Lubrizol) for 48 h, then they were coated on the anode substrate using the drop-coating method before sintering at 1550 and 1450 °C for 4 h for SDC and BCZYYb electrolytes, respectively. For the preparation of cathode ink, the as-prepared YBC-based materials and SDC (and BCZYYb) were composited in a ratio of 6 : 4 wt% with a texanol-based vehicle (type-411, ESL). The composite cathode YBC-SDC and YBC-BCZYYb inks were screen-printed onto the sintered SDC and BCZYYb electrolytes surface, respectively, and then finally sintered at 950 °C for 2 h. Au wires were attached with an Ag mesh using platinum paste (Heraeus, USA) as the current collector.

Electrochemical performance measurements of YBC materials

The electrochemical activity for oxygen electrode reactions in YBC-based materials was evaluated using the polarization resistance (R_p) of the symmetric cells with the SDC measured by electrochemical impedance spectroscopy (EIS) (VSP, Biologic, Claix) from 500 to 800 °C in the frequency range of 1 MHz to 0.1 Hz (10 mV scanning amplitude) under ambient air and open-circuit voltage (OCV) conditions. To further understand the influence of doping YBC on the kinetics of the ORR, the ASR of the symmetric cell with the SDC electrolyte was tested under several oxygen partial pressures (p_{O_2} , from 0.21 to 0.04 atm) at 600–700 °C.

The chemical diffusion (D_{chem}) and surface exchange coefficients (k_{chem}) values for oxygen in the YBC-based materials were determined by electrical conductivity relaxation (ECR) experiments on thin rectangular slabs in a van der Pauw electrode configuration. The samples were prepared by cold-pressing the YBC-based powders then sintering at 1250 °C (for YBC) or 1300 °C (for YEBCG) for 24 h to fabricate a dense bar. DC electrical conductivity was measured using a potentiostat/galvanostat (VSP, Bio-Logic) according to oxygen partial pressure ($-1.98 \leq \log(p_{O_2} \text{ per atm}) \leq -0.68$) that was controlled using a mixture of O₂ and N₂ gas at 600–750 °C. The normalized electrical conductivity (Γ) as a function of time is given by eqn (1);

$$\Gamma \equiv \frac{(\sigma_t - \sigma_0)}{(\sigma_\infty - \sigma_0)} = 1 - \left[\sum_{n=1}^{\infty} \frac{2L^2 \exp\left(-\frac{\beta_n^2 D_{chem}(t - t_0)}{a^2}\right)}{\beta_n^2 (\beta_n^2 + L^2 + L)} \right]^2 \quad (1)$$

$$\beta_n \tan \beta_n = L, \quad L = \frac{ak_{chem}}{D_{chem}} \quad (2)$$

where σ_0 , σ_∞ , and σ_t are the conductivity at the initial moment of the transformed atmosphere, at the final stable time, and at a given time t , respectively. a is the dimension of the sample. D_{chem} and k_{chem} are the chemical diffusion and surface exchange coefficients of oxygen, respectively. The kinetic parameters (D_{chem} and k_{chem}) were obtained from nonlinear least square fits to the solution of the diffusion equation using the ECR data. Further details about the experimental procedures have been described elsewhere.^{37–39}

The anode-supported single cell performance measurements were performed using a fuel cell test station (Scitech Korea) equipped with humidifiers, gas mass flow controllers, and an alumina reactor. Ceramic adhesive (Ceramabond™ 668, Aremco) was used to seal the anode side of the single cells in an alumina tube. Current–voltage (I – V) polarization curve measurements were carried out using a potentiostat/galvanostat (SP-240, BioLogic) under 3 vol% humidified hydrogen and ambient air on the fuel and air electrode side, respectively, at a flow rate of 200 sccm for the SOFC and PCFC. While in PCEC mode, 20% steam mixed with air was fed into the air electrode side using a micro peristaltic pump

(Ismatec). The steam partial pressure was controlled by a temperature-controlled water bubbler. The 10% hydrogen in the wet N_2 stream was fed into the hydrogen electrode side at a flow rate of 200 sccm. The faradaic efficiency of the cells under PCEC operation was measured by analyzing the gas composition of the hydrogen electrode exhaust using gas chromatography.

Density functional theory calculations

All the density functional theory (DFT) calculations were performed using the Vienna *Ab initio* Simulation Package (VASP).⁴⁰ We used projector-augmented wave (PAW) pseudopotentials⁴¹ with a plane-wave basis set as implemented in VASP. Perdew–Burke–Ernzerhof (PBE) parametrization of the generalized gradient approximation (GGA)⁴² was used for the exchange–correlation functional. For the DFT calculations, a $3 \times 2 \times 2$ k -point grid was used to calculate a $1 \times 2 \times 1$ supercell structure of YBC and YBC-based materials. The GGA+U method⁴³ was adopted to address the localization of the d-orbital in Co and each dopant ions, as determined in a previous report.^{44–47} An appropriate number of k -points and a kinetic energy cutoff of 500 eV were used in all the calculations. All the structures were optimized until the force in the unit cell converged to within $0.03 \text{ eV } \text{Å}^{-1}$.

Results and discussion

Structural analysis of YBC-based powders

To evaluate the phase and structure of the as-prepared $YBaCo_4O_{7+\delta}$ (YBC)-based powders, XRD analysis was performed and the results are shown in Fig. 1. The Y-site in the YBC was substituted with various rare-earth metals (Ln = La, Nd, Ce, Gd, Sm, Er, and Yb) to fabricate $Y_{0.9}Ln_{0.1}BaCo_4O_{7+\delta}$ (YLBC) samples. XRD patterns of the synthesized YLBC powders, after using the solid-state reaction method, exhibited a swedenborgite ($NaBe_4SbO_7$) structure without any detectable impurities (except La) (Fig. 1a).⁴⁸ Small traces of impurity phases, such as $La_{0.5}Ba_{0.5}CoO_{3-\delta}$ (PDF#: 32-0480), were detected in the La-doped YBC sample. The transition and post-transition metals (Tr = Fe, Ga, Ni, Mn, Cu, Cr, Al, and Ti), which include the elements in groups 3–12 of the periodic table, were also doped into the Co-site of the YBC to synthesize $YBaCo_{3.6}Tr_{0.4}O_{7+\delta}$ (YBCT) samples. Fig. 1b shows that only $YBaCo_{3.6}Fe_{0.4}O_{7+\delta}$ (YBCF) and $YBaCo_{3.6}Ga_{0.4}O_{7+\delta}$ (YBCG) powders have a pure phase without detectable impurities. Other dopants in the YBCT resulted in the formation of small amounts of impurities, such as $Ba_3Y_4O_9$ (PDF#: 38-1377), Y_2O_3 (PDF#: 43-1036), $YBaCo_2O_5$ (PDF#: 47-0735), and unknown phases.

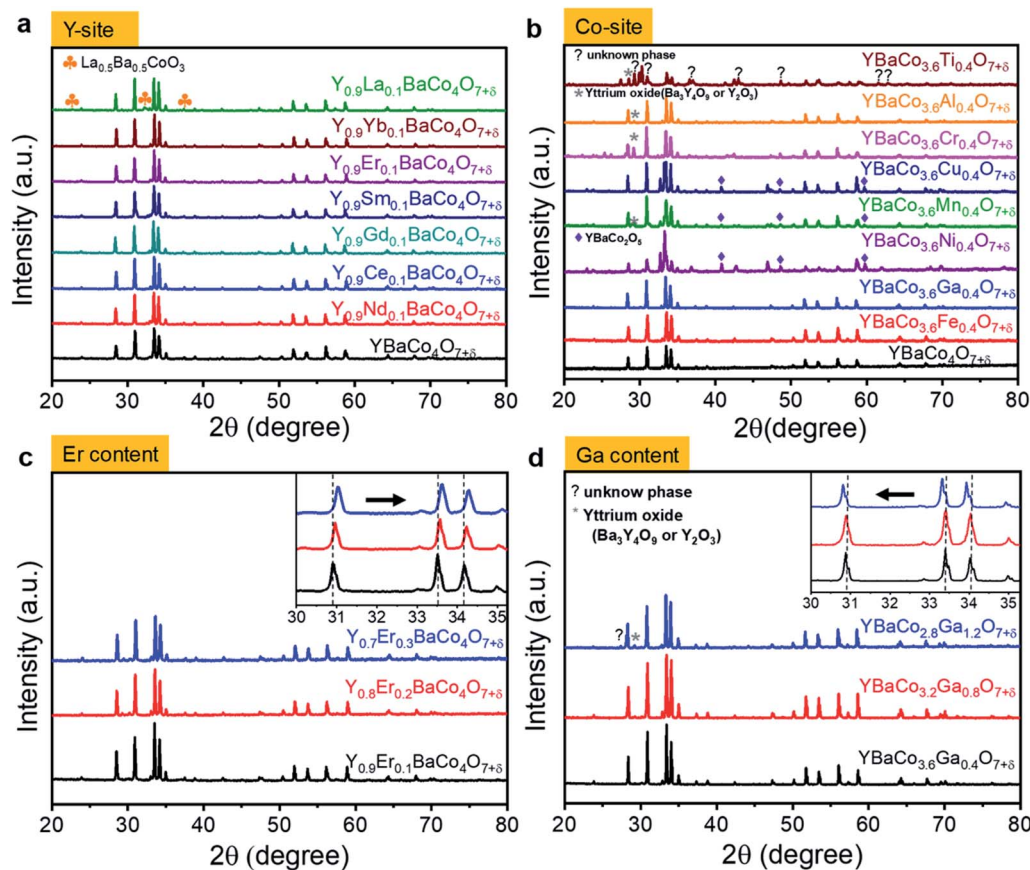


Fig. 1 Phase identification of $Y_{1-x}Ln_xBaCo_{4-y}Tr_yO_{7+\delta}$ powders using XRD. (a) $Y_{0.9}Ln_{0.1}BaCo_4O_{7+\delta}$ (YLBC) doped with lanthanides (Ln = La, Nd, Ce, Gd, Sm, Er, and Yb). (b) $YBaCo_{3.6}Tr_{0.4}O_{7+\delta}$ (YBCT) doped with the transition and post-transition metals (Tr = Fe, Ga, Ni, Mn, Cu, Cr, Al, and Ti). (c) Er-doping in $Y_{1-x}Er_xBaCo_4O_{7+\delta}$ (YEBC, $x = 0.1, 0.2,$ and 0.3). (d) Ga-doping in $YBaCo_{4-y}Ga_yO_{7+\delta}$ (YBCG, $y = 0, 0.4, 0.8,$ and 1.2).

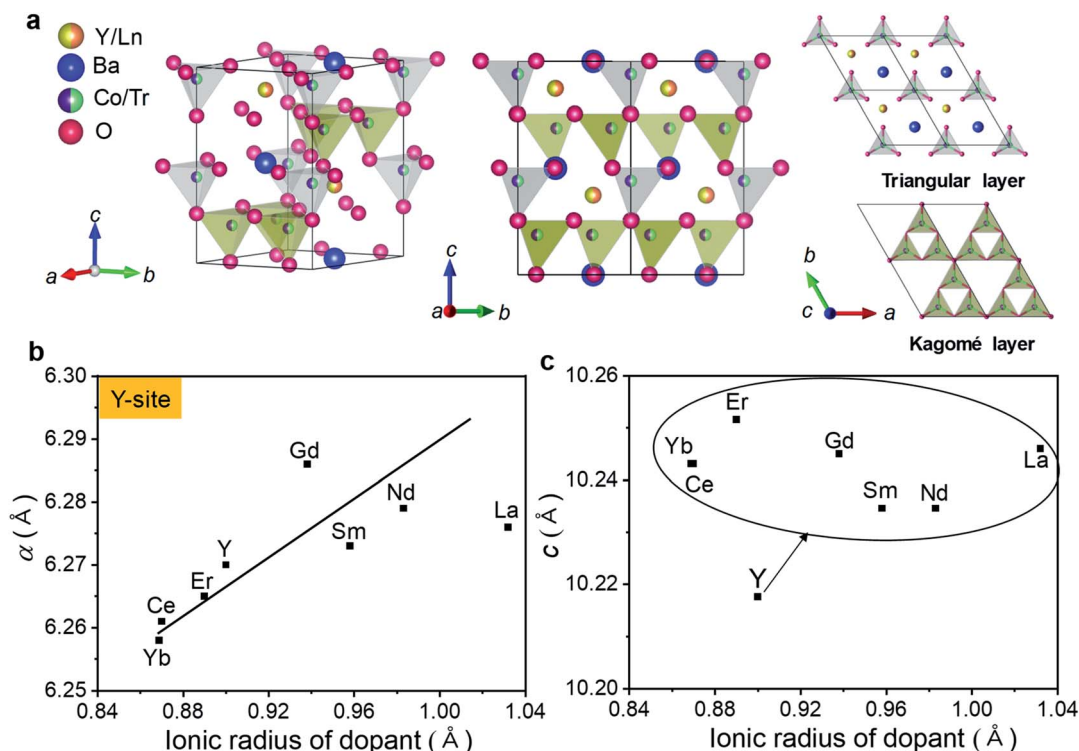


Fig. 2 Structural information of $Y_{1-x}Ln_xBaCo_{4-y}Tr_zO_{7+\delta}$ powders from XRD data. (a) Layered swedenborgite structured $YBaCo_4O_{7+\delta}$ -based compounds. Triangular and Kagomé layers are in the geometrical arrangement of the CoO_4 tetrahedra within a given ab plane. (b and c) Change in the cell parameters of a (b) and c -axes (c) through the addition of dopants in YLBC.

As shown in Fig. 2a, the crystal structures of the YBC, YLBC, and YBCT were indexed as hexagonal structures with a space group of $P6_3mc$, in the agreement with the data seen in literature.^{49,50} The YBC-based oxides, belonging to the swedenborgite compound family, exhibited a special layered crystal structure that consists of an alternating stacking of $Co^{2+/3+}O_4$ tetrahedral layers with Kagomé (6c site) and adjacent triangular (2a site) lattices along the crystallographic c -axis.⁵¹ The oxygen framework can be labelled as hexagonal “ABCB” stacking of close-packed alternating O_4 and BaO_3 layers.⁵² Barium and yttrium cations have 12- and 6-fold coordination with oxygen atoms. In addition, the yttrium cation is likely to be substituted by another cation easily, whereas cobalt is not readily replaced by

other transition metal ions so we see the formation of unwanted impurity phases, as can be seen in Fig. 1a and b.⁵³ In order to provide further insight into the impact of dopants on the YBC structure, the trends in cell parameters of the primary YBC phase for the various samples were analyzed using the XRD data (Tables 1 and 2).

The introduction of new atoms to YBC is expected to lead to changes in cell parameters. As seen in Fig. 2b, the lattice constant of YBC-based materials is linearly increased as the radius of the dopant increases. Lattice parameters a and c are 6.270 and 10.218 Å for YBC. After Y-site doping into YBC, a and c are in the range of 6.258–6.287 and 10.238–10.254 Å for YLBC, respectively, depending on the relative radius of dopants to the

Table 1 Structural information and ASRs of $Y_{0.9}Ln_{0.1}BaCo_4O_{7+\delta}$ ($Ln = La, Nd, Ce, Gd, Sm, Er,$ and Yb) from Rietveld refinements analysis and EIS measurements

Materials (space group: $P6_3mc$, hexagonal)	Lattice parameter		Electro-negativity (dopants)	ASR at 600 °C ($\Omega\text{ cm}^2$)	ASR at 650 °C ($\Omega\text{ cm}^2$)	Activation energy (eV)
	a (Å)	c (Å)				
$YBaCo_4O_{7+\delta}$	6.270 ± 0.001	10.218 ± 0.001	1.22 (Y)	5.588	2.513	1.28
$Y_{0.9}Yb_{0.1}BaCo_4O_{7+\delta}$	6.258 ± 0.001	10.244 ± 0.001	1.10 (Yb)	7.783	2.687	1.40
$Y_{0.9}Ce_{0.1}BaCo_4O_{7+\delta}$	6.261 ± 0.002	10.243 ± 0.001	1.12 (Ce)	5.937	2.400	1.28
$Y_{0.9}Nd_{0.1}BaCo_4O_{7+\delta}$	6.279 ± 0.004	10.238 ± 0.002	1.14 (Nd)	6.001	2.364	1.30
$Y_{0.9}Sm_{0.1}BaCo_4O_{7+\delta}$	6.273 ± 0.003	10.238 ± 0.002	1.17 (Sm)	6.532	2.546	1.34
$Y_{0.9}Gd_{0.1}BaCo_4O_{7+\delta}$	6.287 ± 0.002	10.245 ± 0.001	1.20 (Gd)	4.846	2.143	1.23
$Y_{0.9}Er_{0.1}BaCo_4O_{7+\delta}$	6.265 ± 0.002	10.254 ± 0.002	1.24 (Er)	4.004	1.649	1.24
$Y_{0.9}La_{0.1}BaCo_4O_{7+\delta}$	6.276 ± 0.001	10.246 ± 0.001	1.10 (La)	—	—	—

reflected by changes in the electronic states and bonding states of Co–O, this then influences the electrocatalytic activity of cathode materials in IT-SOFCs.⁵⁴ This will be discussed further in the next section.

Electrical conductivity of YBC-based materials

In order to evaluate the electrocatalytic activity of YBC-based materials for oxygen electrode reactions, electrochemical impedance spectroscopy (EIS) analysis was performed under open-circuit voltage (OCV) conditions in dry air at 500–800 °C. ASRs of the YBC-based materials were measured in symmetrical cells with SDC electrolyte. Fig. 3 shows the Arrhenius plot of ASR *versus* temperature for the YBC-based materials. In the case of Y-site doping in the YBC (Fig. 3a), the $Y_{0.9}Er_{0.1}BaCo_4O_{7+\delta}$ cell substituted with Er^{3+} exhibited lower ASR than that of YBC and other doped YBC materials in all temperature ranges. In addition, using Gd^{3+} and Er^{3+} as dopants for the Y-site was very effective in decreasing the ASR of YBC at IT, whereas the $Y_{0.9}Sm_{0.1}BaCo_4O_{7+\delta}$ (YSBC) and $Y_{0.9}Yb_{0.1}BaCo_4O_{7+\delta}$ (YYBC) with Sm^{3+} and Yb^{3+} dopants showed higher ASRs than YBC.

It is interesting to note that the ASR of YLBC materials tends to increase with the electronegativity of cations at 600 °C, as shown in Fig. 3b. In particular, Er, which possesses a higher electronegativity (1.24) than other rare-earth metals, exhibits the lowest ASR with the lowest activation of 1.24 eV, among the various rare-earth oxide dopants (Table 1). These results may come from the fact that the doping of high electronegativity cations in the Y-site is likely to increase the covalent character of YLBC. That is, the electronegativity of Er strongly attracts nearby electrons in the crystal structure due to the significantly high electronegativity of Co (1.88) and O (3.44), allowing more electrons to share with the Co–O bond. In addition, Suntivich *et al.*⁵⁵ and Shao-Horn *et al.*⁵⁶ reported that increased covalency in the M–O bond facilitates charge transfer between surface cations and adsorbates such as O^{2-} and O_2^{2-} for ORR, which can result in lower ASRs of cathode materials. In contrast, it was not easy to find any correlation between the electrical conductivity and cell parameters (Fig. S1†).

To investigate the doping of transition and post-transition metal oxides in to the Co-sites of YBC, the ASRs of YBCF- and YBCG-based symmetrical cells with SDC electrolyte were also

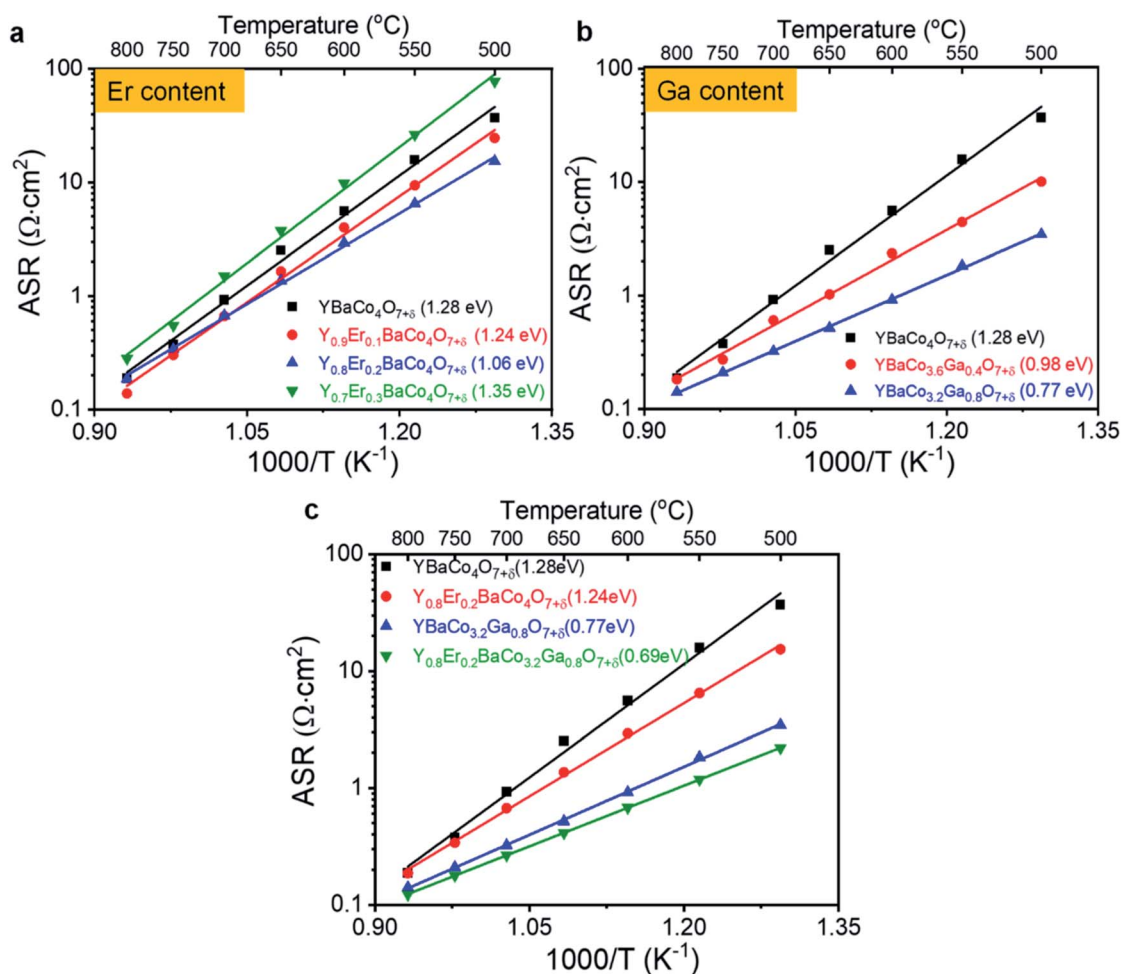


Fig. 4 Electrocatalytic activity measurements of $Y_{1-x}Ln_xBaCo_{4-y}Tr_yO_{7+\delta}$ symmetric cells with the activation energy for oxygen electrode reactions from EIS. (a) Arrhenius plot of ASRs of $Y_{1-x}Er_xBaCo_4O_{7+\delta}$ ($x = 0.1, 0.2, \text{ and } 0.3$). (b) Arrhenius plot of ASRs of $YBaCo_{4-y}Ga_yO_{7+\delta}$ ($y = 0, 0.4, \text{ and } 0.8$). (c) Arrhenius plot of ASRs of $Y_{0.8}Er_{0.2}BaCo_{3.2}Ga_{0.8}O_{7+\delta}$ (YBECG).

determined by EIS measurements under OCV conditions in dry air at 500–800 °C and the results are presented in Fig. 3c (Fig. S2†). The EIS results for the other transition and post-transition metals oxide cells are not presented here because of the impurity phases that accompanied the doping process. In the case of Co-site doping into the YBC, the $\text{YBaCo}_{3.6}\text{Ga}_{0.4}\text{O}_{7+\delta}$ (YBCG) cell substituted with Ga^{3+} exhibited lower ASRs than YBC or $\text{YBaCo}_{3.6}\text{Fe}_{0.4}\text{O}_{7+\delta}$ (YBCF) at IT. Interestingly, the ASRs of YBCT materials decreased linearly with the increase in the cell parameters at 600 °C, as shown in Fig. 3d. In particular, Ga (YBCG), which has a larger structural parameter than other transition metal oxides (YBCT), demonstrates the lowest ASRs (Table 2). This increase is simply due to the large cell parameters of YBCG; the wider the lattice and the larger the spaces in a structure, the faster it is for oxide ions to transport through the lattice. In addition, the different oxidation states of the substituents may contribute to improve the ASR of YBCT with the modification of the average Co valence, this would affect the mixed ionic and electronic conductivity of YBC-based materials.

Er and Ga doped YBC materials

We investigate the synergistic effects of two dopants (Er and Ga) in the Y- and Co-sites on the performance of a swedenborgite

structured YBC cathode. First, to optimize the concentration of Er-doping in $\text{Y}_{1-x}\text{Er}_x\text{BaCo}_4\text{O}_{7+\delta}$ (YEBC, $x = 0.1, 0.2,$ and 0.3), the YEBC was synthesized using the solid-state reaction method. The diffraction peaks from the Y-site substituted YEBC with the different concentrations of Er appeared as a single phase without any secondary phase, as shown in Fig. 1c. A slight shift in the XRD peaks towards a higher 2θ for YEBC was observed with increasing Er content (inset of Fig. 1c), indicating that the lattice parameter does decrease slightly, this is because the Er^{3+} (0.89 Å) has a smaller ionic radius than Y^{3+} (0.90 Å).

ASRs of the YEBC materials with various Er concentration were determined by EIS and the results are presented in Fig. 4a. 20 mol% Er-doped YBC ($\text{Y}_{0.8}\text{Er}_{0.2}\text{BaCo}_4\text{O}_{7+\delta}$) reveals the lowest ASRs in the intermediate temperature range (500–700 °C) among the Er-doped YBC materials. In addition, the activation energies of YBC, $\text{Y}_{0.9}\text{Er}_{0.1}\text{BaCo}_4\text{O}_{7+\delta}$, $\text{Y}_{0.8}\text{Er}_{0.2}\text{BaCo}_4\text{O}_{7+\delta}$, and $\text{Y}_{0.7}\text{Er}_{0.3}\text{BaCo}_4\text{O}_{7+\delta}$, calculated from Arrhenius equation, were 1.28, 1.24, 1.06, and 1.35 eV, respectively, in the SDC electrolyte symmetrical cell. That is, the oxygen electrode activity increases with increasing Er in the YEBC materials. However, the ASR of the $\text{Y}_{0.7}\text{Er}_{0.3}\text{BaCo}_4\text{O}_{7+\delta}$ cathode material is lower than that of $\text{Y}_{0.8}\text{Er}_{0.2}\text{BaCo}_4\text{O}_{7+\delta}$ with significantly higher activation energy. The decreased oxygen electrode activity for high concentrations

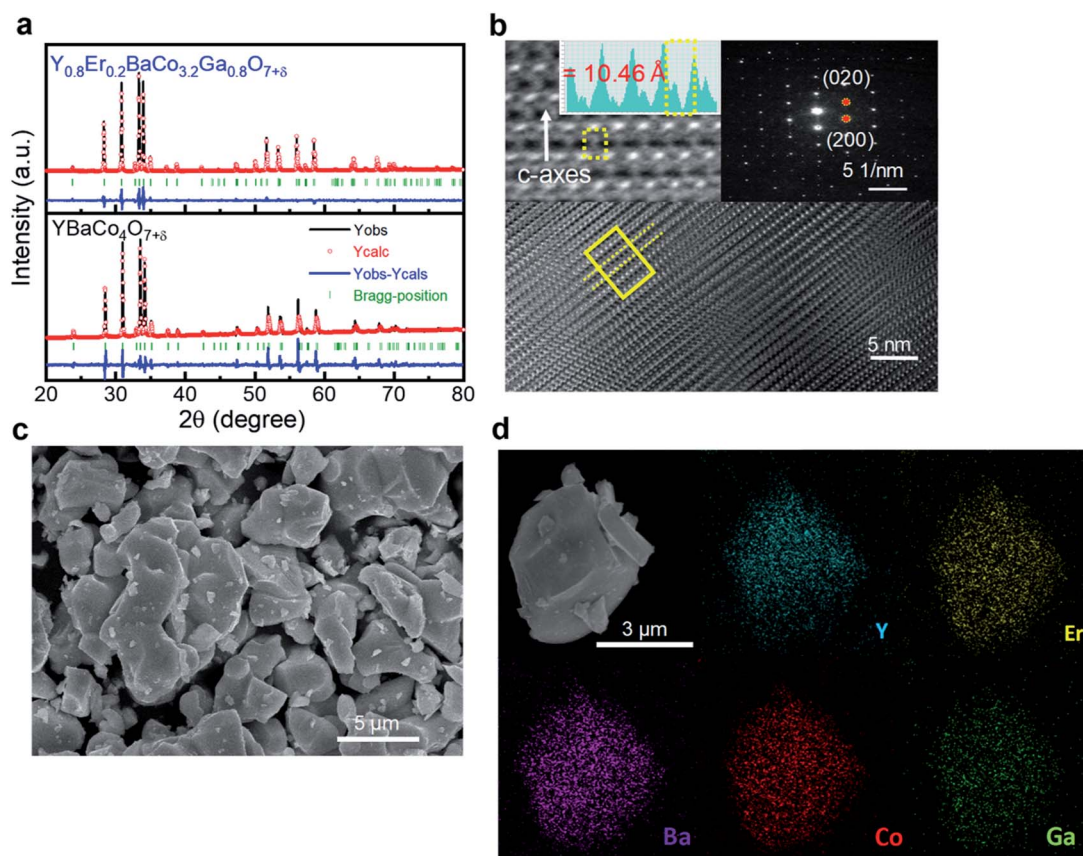


Fig. 5 Characterizations of YEBCG powders by XRD, FESEM, and TEM/EDX. (a) XRD results with Rietveld refinement ($R_{\text{wp}} = 2.37\%$, $R_p = 1.24\%$, and $\chi^2 = 6.16$ for YEBCG, $R_{\text{wp}} = 3.31\%$, $R_p = 1.71\%$, and $\chi^2 = 7.83$ for YBC). (b) HRTEM image with selected area electron diffraction (SAED) pattern. The inset shows an atomic resolution image of white dotted parallel lines with an observed unit cell and the line profile along c direction in the SAED pattern. (c) FESEM morphology. (d) HRTEM/EDX elemental mapping.

of Er doping might result from a slight phase instability or from defect interactions due to different dopant cations.

Second, the Ga-doped YBC materials ($\text{YBaCo}_{4-y}\text{Ga}_y\text{O}_{7+\delta}$, YBCG) were fabricated with various Ga contents ($y = 0, 0.4, 0.8$, and 1.2) to find the best composition for ASRs when used as a cathode material. The XRD patterns of the $\text{YBaCo}_{3.6}\text{Ga}_{0.4}\text{O}_{7+\delta}$, $\text{YBaCo}_{3.2}\text{Ga}_{0.8}\text{O}_{7+\delta}$, and $\text{YBaCo}_{2.8}\text{Ga}_{1.2}\text{O}_{7+\delta}$ powders with the Rietveld refinement results are shown in Fig. 1d. Both the $\text{YBaCo}_{3.6}\text{Ga}_{0.4}\text{O}_{7+\delta}$ and $\text{YBaCo}_{3.2}\text{Ga}_{0.8}\text{O}_{7+\delta}$ formed single swedenborgite phases, whereas the $\text{YBaCo}_{2.8}\text{Ga}_{1.2}\text{O}_{7+\delta}$ powder exhibited a minor secondary phase of yttrium oxides, such as $\text{Ba}_3\text{Y}_4\text{O}_9$ and Y_2O_3 , implying the solubility limit of Ga dopant in YBCG was reached. Interestingly, in contrast to the peak shift in the XRD patterns for the Y-site substituted YBCs with different Er concentrations, the YBCG exhibited a shift towards a lower 2θ angle with increasing Ga concentration (inset of Fig. 1d), indicating the increasing of cell parameters with the Ga doping. The electrochemical activity of YBCG towards oxygen electrode reactions was measured by EIS in ambient air, the ASRs are presented in Fig. 4b. The activity increases with increasing levels of Gd dopant, this is accompanied by decreasing activation energy for oxygen electrode reactions. The activation energies of YBC, $\text{YBaCo}_{3.6}\text{Ga}_{0.4}\text{O}_{7+\delta}$, and $\text{YBaCo}_{3.2}\text{Ga}_{0.8}\text{O}_{7+\delta}$ were also calculated as 1.28, 0.98, and 0.77 eV, indicating that Ga doping facilitates the kinetics for ORR/OER really well as a result of the increased cell parameters, as mentioned in the previous section.

Third, we investigate the impact of co-doping of Er^{3+} and Ga^{3+} in YBC materials on oxygen electrode activity. Er- and Ga-doped YBC materials ($\text{Y}_{0.8}\text{Er}_{0.2}\text{BaCo}_{3.2}\text{Ga}_{0.8}\text{O}_{7+\delta}$, YEBCG) were synthesized using the solid-state reaction method. Fig. 5a shows the XRD results for the YEBCG powders with Rietveld refinement to obtain accurate structural information. The low reliability factors (e.g. $R_{\text{wp}} = 2.37\%$, $R_{\text{p}} = 1.24\%$) for YEBCG indicate good fitting between the experimental and calculated XRD patterns with a goodness-of-fit (χ^2) of 6.16. The XRD patterns confirm the crystallization into a swedenborgite structure after calcinations. Table 3 lists the Rietveld analysis of YEBCG. The Rietveld refinement shows that all compounds crystallized in to a hexagonal structure with the space group $P6_3mc$, indicating that the space group symmetry of YBC does not change with the substitution of Er and Co.^{49,50} However, an increase in the structural parameters (a and c) was observed, a went from 6.270 to 6.304 Å and c went from 10.218 to 10.263 Å.

This led to an increase in the unit cell volume from 347.897 \AA^3 (for YBC) to 353.223 \AA^3 (for YEBCG).

In order to further understand the structure of YEBCG, HRTEM and FESEM examinations were performed. The swedenborgite structure in the YEBCG was confirmed with the selected area electron diffraction (SAED) pattern from the HRTEM image (Fig. 5b). Inset of Fig. 5b shows the representative points in the SAED pattern, which can be indexed as (020) and (200) reflections along the [001] zone axis of YEBCG, this is in agreement with the results obtained from Rietveld refinement (Table 3). Fig. 5c and d display the FESEM morphology of the YEBCG powders with HRTEM/EDX elemental mapping. The YEBCG shows an agglomerated spherical particle morphology 1–4 μm in size because of the high calcination temperature (1200 °C for 12 h) used in the conventional solid-state reaction method. Compositional mapping images of YEBCG confirmed that the all the constituent cations, Y, Er, Ba, Co, and Ga, are homogeneously distributed without any observable elemental segregation in the EDX analysis.

To look into the effects of co-doping in the YEBCG materials on electrocatalytic activity for oxygen electrode reactions, the ASR was measured by EIS under OCV in ambient air with a symmetrical cell. Fig. S3a† exhibits the Nyquist complex plane of YEBCG at 500–800 °C. Two parallel R - Q circuits were used to fit the EIS data, where R_{ohmic} , R_{HF} , and R_{LF} represent the ohmic, charge transfer (HF; high frequency), and mass transfer (LF; low frequency) resistances of the cells, respectively, where Q_2 and Q_3 represent the constant phase elements. As shown in Fig. 4c, YEBCG exhibits lower ASRs in all measured temperature ranges compared to YBC, $\text{Y}_{0.8}\text{Er}_{0.2}\text{BaCo}_4\text{O}_{7+\delta}$, and $\text{YBaCo}_{3.2}\text{Ga}_{0.8}\text{O}_{7+\delta}$, suggesting the co-doping of Er and Ga effectively enhanced the ORR electrocatalytic activity. In addition, the activation energy of YEBCG was considerably decreased from 1.28, 1.06, and 0.77 eV for YBC, $\text{Y}_{0.8}\text{Er}_{0.2}\text{BaCo}_4\text{O}_{7+\delta}$, $\text{YBaCo}_{3.2}\text{Ga}_{0.8}\text{O}_{7+\delta}$, respectively, to 0.69 eV, indicating that the co-doping of Er and Co impressively expedites the kinetics for ORR/OER (Table 3). Furthermore, the YEBCG outperformed the other perovskite structured cathode materials at intermediate temperatures. For example, the ASR of YEBCG was $0.413 \Omega \text{ cm}^2$ at 650 °C, and it was much lower than that of LSCF⁵⁷ and SSC,⁵⁸ implying its appropriateness for triggering oxygen electrode reactions at intermediate temperatures (Fig. S3b†). Fig. S3c† shows the electrical conductivity of the YEBCG in the temperature range of 300–800 °C. The YEBCG demonstrated excellent electrical

Table 3 Structural information and ASRs of $\text{Y}_{1-x}\text{Er}_x\text{BaCo}_4\text{O}_{7+\delta}$ ($x = 0.2$ and 0.3), $\text{YBaCo}_{4-y}\text{Ga}_y\text{O}_{7+\delta}$ ($y = 0.8$ and 1.2), and $\text{Y}_{0.8}\text{Er}_{0.2}\text{BaCo}_{3.2}\text{Ga}_{0.8}\text{O}_{7+\delta}$

Materials (space group: $P6_3mc$, hexagonal)	Lattice parameter		ASR at 600 °C ($\Omega \text{ cm}^2$)	ASR at 650 °C ($\Omega \text{ cm}^2$)	Activation energy (eV)
	a (Å)	c (Å)			
$\text{Y}_{0.8}\text{Er}_{0.2}\text{BaCo}_4\text{O}_{7+\delta}$	6.254 ± 0.001	10.235 ± 0.001	2.933	1.366	1.06
$\text{Y}_{0.7}\text{Er}_{0.3}\text{BaCo}_4\text{O}_{7+\delta}$	6.248 ± 0.001	10.212 ± 0.002	9.792	3.745	1.35
$\text{YBaCo}_{3.2}\text{O}_{0.8}\text{GaO}_{7+\delta}$	6.303 ± 0.001	10.262 ± 0.001	0.917	0.517	0.77
$\text{YBaCo}_{2.8}\text{O}_{1.2}\text{GaO}_{7+\delta}$	6.307 ± 0.001	10.266 ± 0.001	—	—	—
$\text{Y}_{0.8}\text{Er}_{0.2}\text{BaCo}_{3.2}\text{Ga}_{0.8}\text{O}_{7+\delta}$	6.304 ± 0.003	10.263 ± 0.002	0.680	0.413	0.69

conductivity ($1.4\text{--}2.7\text{ S cm}^{-1}$) at intermediate temperatures ($500\text{--}700\text{ }^\circ\text{C}$).

Oxygen electrode reaction activity of YEBCG

To analyze the oxygen electrode reaction step and understand electrochemical kinetics of YEBCG, EIS measurements of the symmetric cell were performed at various temperatures and with the $p\text{O}_2$ as seen in Fig. 6. It can be seen that the polarization resistance (R_p) decreases linearly with increasing $p\text{O}_2$ on a logarithmic scale, indicating that the ORR process is strongly affected by the oxygen concentration. The slope of the $\log R_p$ for YEBCG was calculated as a function of $\log p\text{O}_2$ (in the relation $R_p \propto p\text{O}_2^{-n}$) to estimate the rate-determining step (RDS) of the ORR process on the cathode.⁵⁹ The oxygen activity for the cathode involves oxygen adsorption, dissociation, surface diffusion, and charge-transfer processes, how these processes occur is closely related to both the cathode's surface and bulk properties.⁶⁰ For $n = 1/4$, the RDS is generally attributed to the charge transfer process at the cathode interface ($\text{O}_{2\text{ads}} + 2\text{e}^- + \text{V}_\text{O}^{\bullet\bullet} \rightleftharpoons 2\text{O}_\text{O}^{\times}$), while $n = 1/2$ is typically associated with the mass transfer processes such as surface oxygen

adsorption and dissociation ($\text{O}_{2\text{ads}} \rightleftharpoons 2\text{O}_{\text{ads}}$). As shown in Fig. 6a and b, the n slopes of R_{HF} and R_{LF} turn up at around $n = 1/4$ and $1/2$, respectively, indicating that the ORR at high frequency corresponds to the charge transfer process, whereas the RDS at low frequency is related to the oxygen adsorption and dissociation process. It should be noted that R_{HF} is always smaller than R_{LF} for various $p\text{O}_2$ at $600\text{--}700\text{ }^\circ\text{C}$, this specifies that the RDS for the ORR is the diffusion process, on the other hand, the charge transfer of YEBCG is greatly improved.

Furthermore, the kinetic properties for ORR/OER can be related to the bulk diffusion and surface exchange properties of oxygen.⁶¹ The chemical bulk diffusion (D_{chem}) and surface exchange coefficients (k_{chem}) of YEBCG were determined from the measurement of the transient response to a step change in $p\text{O}_2$ by the electrical conductivity relaxation (ECR) method (Fig. S4†).⁶² Both D_{chem} and k_{chem} values for YEBCG were much faster than those for other perovskite structured materials in the temperature range studied ($600\text{--}750\text{ }^\circ\text{C}$), as can be seen in Fig. 6c and d. As an example, D_{chem} and k_{chem} of YEBCG were 7.12×10^{-4} and $8.01 \times 10^{-3}\text{ cm}^2\text{ s}^{-1}$, respectively, at $650\text{ }^\circ\text{C}$, this is much higher than those of $\text{Ba}_{0.5}\text{Sr}_{0.5}\text{Co}_{0.8}\text{Fe}_{0.2}\text{O}_{3-\delta}$

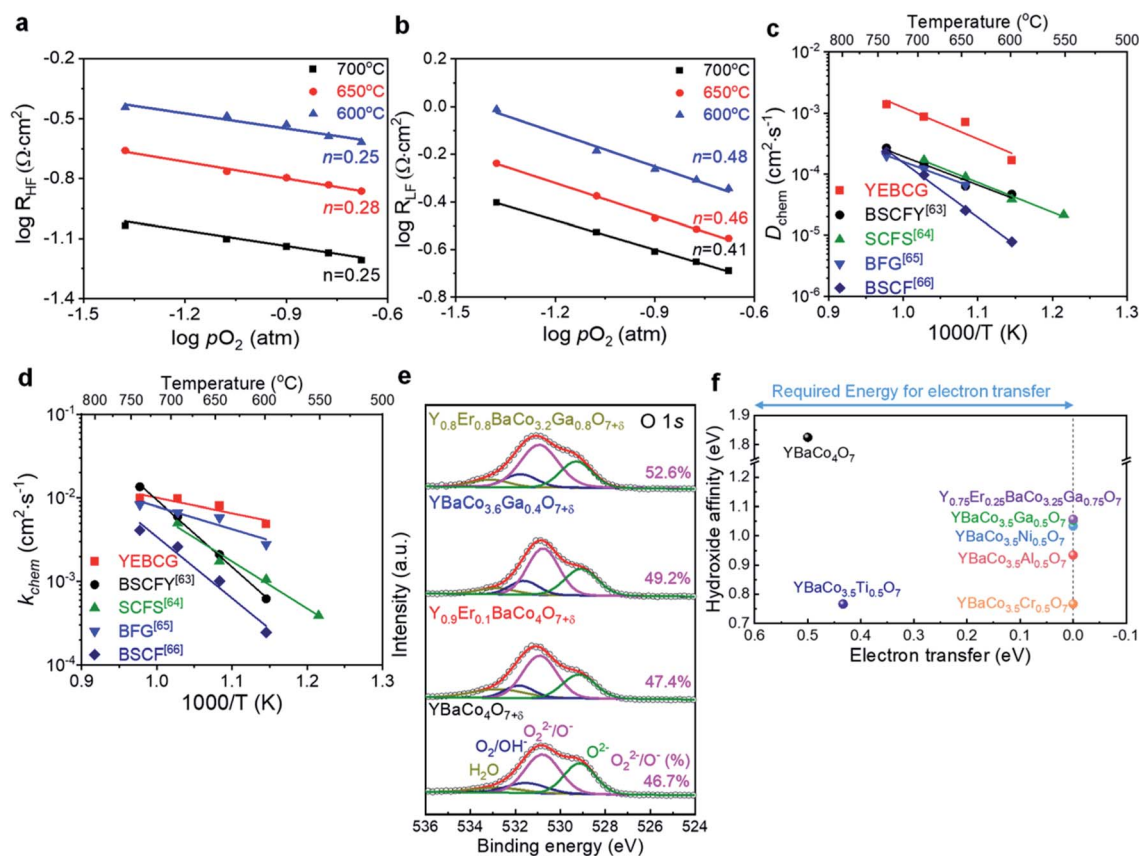


Fig. 6 EIS measurements of YEBCG symmetric cells, analysis of oxygen species existing on the air electrode surface by O 1s XPS spectra, and DFT calculations. (a and b) Polarization resistance (R_p) as a function of $p\text{O}_2$ on the logarithmic scale at high frequency (HF) (a) and at low frequency (LF) (b) at $600\text{--}700\text{ }^\circ\text{C}$ for ORR process. (c and d) Chemical bulk diffusion (D_{chem}) (c) and surface exchange coefficients of oxygen (k_{chem}) (d) determined from the measurement of the transient response to a step change in $p\text{O}_2$ at $550\text{--}750\text{ }^\circ\text{C}$ using the ECR method with a comparison to other perovskite materials [$\text{Ba}_{0.5}\text{Sr}_{0.5}\text{Co}_{0.8}\text{Fe}_{0.2}\text{O}_{3-\delta}$ (BSCF), $\text{Ba}_{0.5}\text{Sr}_{0.5}\text{Co}_{0.8}\text{Fe}_{0.175}\text{Y}_{0.025}\text{O}_{3-\delta}$ (BSCFY), $\text{BaFe}_{0.975}\text{Gd}_{0.25}\text{O}_{3-\delta}$ (BFG), and $\text{SrCo}_{0.6-\text{Fe}_{0.3}\text{Sn}_{0.1}\text{O}_{3-\delta}$ (SCFS)]. (e) Relative contents of oxidative oxygen species in the YBC-based materials. (f) Theoretical oxygen electrode properties for ORR/OER of $\text{Y}_{1-x}\text{Er}_x\text{BaCo}_{4-y}\text{Tr}_y\text{O}_{7+\delta}$ ($x = 0.25$; $y = 0.5$ and 0.75 ; $\text{Tr} = \text{Ga}, \text{Ni}, \text{Cr}, \text{Al},$ and Ti) using first-principles calculation.

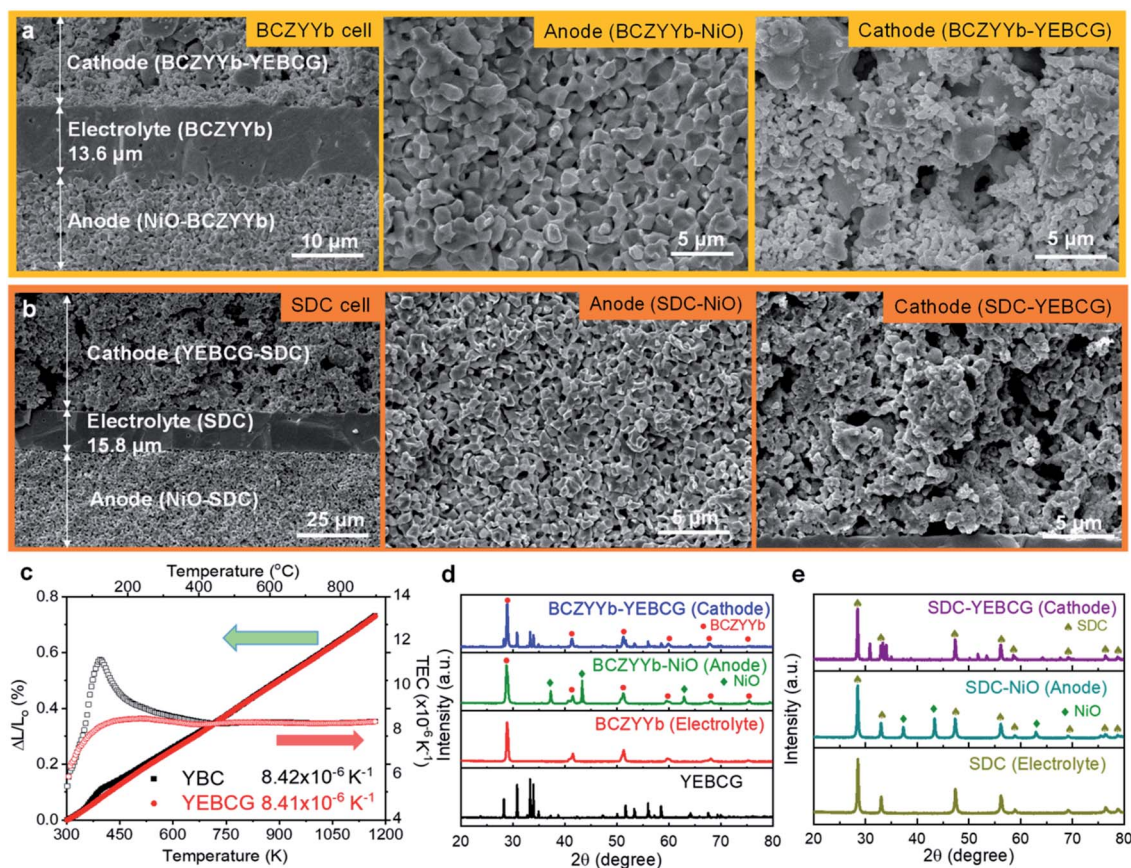


Fig. 7 Characterizations of anode-supported YBCG cells. (a and b) Cross-sectional FESEM analyses of NiO-BCZYYb supported YBCG cell for RPCCs (a) and NiO-SDC supported YBCG cell for SOFCs with anode and cathode surface morphologies. (c) Variation of $\Delta L/L_0$ as a function of temperature of YBC and YEBCG materials measured by dilatometer. (d) XRD patterns of NiO-BCZYYb anode-supported cell components. (e) XRD patterns of NiO-SDC anode-supported cell components.

(BSCF, 2.52×10^{-5} and 1.01×10^{-3} $\text{cm}^2 \text{s}^{-1}$), $\text{Ba}_{0.5}\text{Sr}_{0.5}\text{Co}_{0.8}\text{Fe}_{0.175}\text{Y}_{0.025}\text{O}_{3-\delta}$ (BSCFY, 6.30×10^{-5} and 2.10×10^{-3} $\text{cm}^2 \text{s}^{-1}$), $\text{BaFe}_{0.975}\text{Gd}_{0.25}\text{O}_{3-\delta}$ (BFG, 6.67×10^{-5} and 5.81×10^{-3} $\text{cm}^2 \text{s}^{-1}$), and $\text{SrCo}_{0.6}\text{Fe}_{0.3}\text{Sn}_{0.1}\text{O}_{3-\delta}$ (SCFS, 9.0×10^{-5} and 1.75×10^{-3} $\text{cm}^2 \text{s}^{-1}$ for D_{chem} and k_{chem} , respectively at 650°C).^{63–66}

Upon doping YBC with atoms of different oxidation states and ionic radii, changes in the interatomic spacings due to local lattice distortions are eventually related to modifications in the electronic and bonding states of Co–O, this influences the electrocatalytic activity of the air electrode materials for SOFCs and RPCCs, as mentioned earlier. The population of mobile oxygen defects has been also found to profoundly influence the oxygen electrode reaction kinetics associated with oxygen bulk diffusion and surface exchange of cathode materials. There are different kinds of oxygen species existing on the cathode surface, which is important to the ORR/OER process. As shown in Fig. 6e, the four strong peaks centering at approximately 529.1, 530.8, 531.7, and 532.9 eV can be designated as 4 lattice oxygen species (O^{2-}), highly oxidative oxygen species ($\text{O}_2^{2-}/\text{O}^-$), surface adsorbed oxygen (O_2/OH^-), and molecular water adsorbed on the surface (H_2O), respectively.⁶⁷ The formation of a highly active oxy(hydroxide) surface layer, which is correlated with the surface oxygen defects of the materials, can be

favorable to the OH^- adsorption kinetics and electron transport properties for ORR/OER.⁶⁸ The relative content of highly oxidative oxygen species on the YEBCG surface (52.6%) was estimated from the integrated area ratios of the sub-peaks, this is obviously higher than in YBC (46.7%), YEBC (47.4%), and YBCG (49.2%), demonstrating that YEBCG is highly electrocatalytically active for ORR/OER.

The co-doping effect of YBC-based materials was further investigated using the first-principles calculation. In oxygen electrode process for ORR/OER, electron-transfer energy refers to the required energy value when electrons move from the redox potential of electrolyte to the conduction band of the oxide, and is commonly known as a Schottky barrier. As the electron-transfer energy decreases, the energy required for electrons to diffuse at the oxide/electrolyte interface also decreases, which results in enhanced ORR/OER activity.⁶⁹ Moreover, hydroxide-affinity is related to the Fermi level (E_f) of oxide.⁷⁰ When the Fermi level of the oxide is lower than the redox potential of the electrolyte, the surface of the oxide is negatively charged to balance the electrolyte interface. These charged oxides can attract hydroxide ions from the electrolyte, and when these potential differences are large, the chemical interaction of ORR/OER also increases. Thus, theoretical ORR/

OER properties of the oxide, such as electron transfer and hydroxide affinity, can be derived from their projected DOS (pDOS) of oxygen and transition metal ions.⁷⁰ As presented in Fig. 6f, we calculated the pDOS of $Y_{1-x}Er_xBaCo_{4-y}Tr_yO_{7+\delta}$ ($x = 0.25$; $y = 0.5$ and 0.75 ; $Tr = Al, Cr, Ga, Ni$ and Ti) structures. Their full DOS are illustrated in Fig. S5†. It was predicted that pristine YBC exhibits high hydroxide affinity but high electron-transfer, which implies that pristine YBC is not suitable for

oxygen electrode process for ORR/OER. Most of Co-site doped YBCT, on the other hand, delivered negligible Schottky barrier compared to pristine YBC, which indicates facile electron diffusion from electrolyte to oxide at Co-site doped YBCT compared to pristine YBC. In particular, YEB CG exhibited excellent oxygen catalytic properties compared to the other samples, indicating that the calculated results were consistent with experimental results.

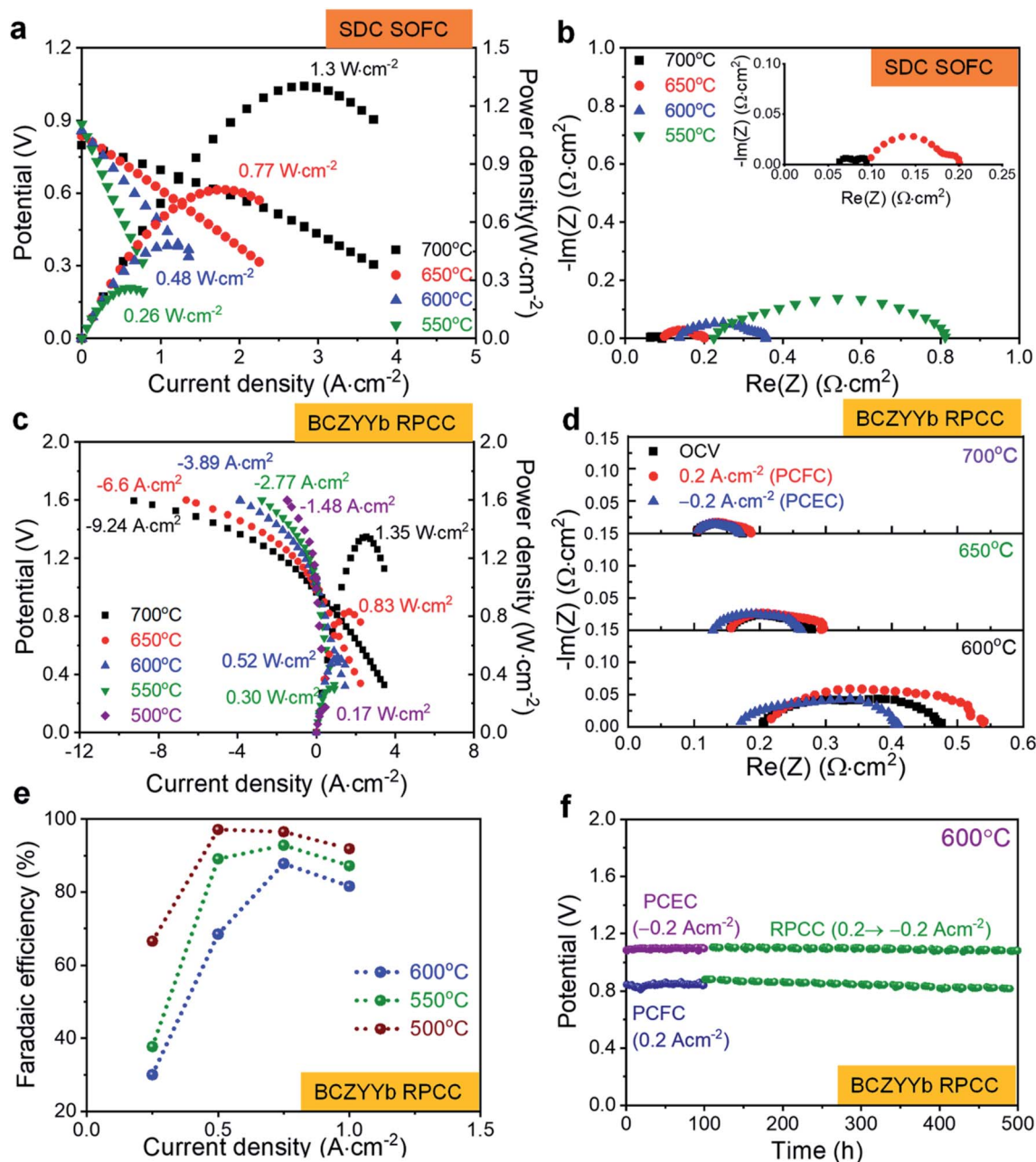


Fig. 8 Electrochemical performance of the swedenborgite structured YEB CG cells at 550–700 °C. (a and b) Current–voltage polarization curves (a) and EIS spectra (b) of anode-supported NiO–SDC cells with the YEB CG cathode under SOFC mode. The inset shows a magnified EIS spectra of the high frequency range. (c and d) Current–voltage polarization curves (c) and EIS spectra (d) of anode-supported NiO–BCZYYb RPCCs with the YEB CG air electrode in PCFC (3% humidified H₂ and ambient air) and PCEC modes (20% steam in air and 10% H₂/90% N₂ in fuel electrodes). (e) Faradaic efficiency of YEB CG RPCCs as a function of current density and temperature. (f) Long-term durability of YEB CG RPCCs over 1000 h under a constant voltage of 0.2 (PCFC) and –0.2 A cm⁻² (PCEC).

Electrochemical performances and durability of the YEBCG cell

To verify the excellent performance of YEBCG for ORR/OER, NiO-BCZYYb and NiO-SDC anode-supported cells were fabricated using the tape-casting method. The NiO-BCZYYb (SDC) anode-supported cells mainly consist of anode substrate, electrolyte (BCZYYb, SDC), and composite cathode (YEBCG-BCZYYb, YEBCG-SDC), as characterized using FESEM in Fig. 7a and b. The dense BCZYYb (SDC) electrolyte was deposited on the porous anode substrate with a thickness of ~ 13.6 (15.8) μm . The composite YEBCG-BCZYYb (SDC) cathode was attached to the electrolyte in a uniform manner with sufficiently porous fine particles. The good wettability of the cathode layer with the electrolyte may be due to the similar thermal expansion coefficient (TEC) values between YEBCG and BCZYYb (SDC). As shown in Fig. 7c, the TEC values for the YEBCG is $8.41 \times 10^{-6} \text{ K}^{-1}$, which is relatively close to that of BCZYYb ($9.5 \times 10^{-6} \text{ K}^{-1}$) and SDC electrolyte ($12.8 \times 10^{-6} \text{ K}^{-1}$).^{25,71} Furthermore, the YEBCG has advantages in terms of long-term thermal stability since large thermal mismatch of cell components can create critical mechanical stress between interfaces.

The phase purities of the cell components were investigated by XRD (Fig. 7d and e). The tape-casted NiO-BCZYYb (SDC) anode substrate show the pure NiO and cubic perovskite (fluorite) structure of BCZYYb (SDC) phases with no unwanted impurities. The XRD diffractograms for the BCZYYb (SDC) electrolyte clearly demonstrate that the powders are comprised of the perovskite phase. The XRD patterns for the composite YEBCG-BCZYYb (SDC) reveal all the major characteristic peaks of YEBCG swedenborgite and BCZYYb perovskite (SDC fluorite) structures without any detectable impurity peaks after annealing at a high temperature of 950 °C for 2 h.

The electrochemical performance of the YEBCG cells was measured at 500–700 °C using humidified hydrogen (3 vol%) on the anode side and ambient air on the cathode side for SOFCs and PCFCs. *I-V-P* curves of the YEBCG cell (with SDC electrolyte) in an SOFC are presented in Fig. 8a. The open-circuit voltage (OCV) values of the YEBCG cell were 0.799–0.887 V at 550–700 °C. The low OCV of the cells is because of the reduction of the thin SDC electrolyte under a reducing atmosphere, despite the fact the SDC layers were dense without any pinholes. The maximum power densities (MPDs) of the YEBCG cell were 0.48, 0.77, 1.30 W cm^{-2} at 600, 650, and 700 °C, respectively. At 550 °C, the MPD of the YEBCG cell was 0.26 W cm^{-2} . Fig. 8b displays the EIS plots of YEBCG cell under OCV at 550–700 °C. The R_{ohmic} and R_{p} of YEBCG cell decreased with increasing temperature from 550 to 700 °C due to the thermally activated processes that occur. The ohmic ASR was 0.064–0.225 $\Omega \text{ cm}^2$ at 700–550 °C; the electrode ASR was 0.033–0.587 $\Omega \text{ cm}^2$ at these temperatures.

In PCFC mode under RPCC operation, the high OCVs of the cells (1.05 and 1.02 V at 550 and 650 °C, respectively) can be seen in Fig. 8c, this demonstrates that the electrolyte is dense. The MPDs of the cell were 0.30, 0.52, 0.83, and 1.35 W cm^{-2} at 550, 600, 650, and 700 °C, respectively. The ohmic and electrode ASRs were 0.152–0.289 and 0.07–0.592 $\Omega \text{ cm}^2$, respectively,

under OCV at 700–550 °C, according to the EIS results shown in Fig. 8d and S6.† The YEBCG RPCCs were also tested in PCEC mode at 500–700 °C. 20% steam in ambient air and 10% H_2 in a wet N_2 stream were supplied to the steam and fuel electrode, respectively. The YEBCG RPCC achieved remarkably high current densities of -0.61 , -1.75 and -4.42 A cm^{-2} at 500, 600 and 700 °C, respectively, at an applied voltage of 1.4 V. The electrode ASRs under -0.2 A cm^{-2} in PCEC mode were 0.066, 0.128 and 0.239 $\Omega \text{ cm}^2$ at 700, 650 and 600 °C, respectively, these are considerably lower than those obtained in PCFC mode. Moreover, faradaic efficiency of YEBCG cell was measured at 500, 550, and 600 °C, respectively, at an applied current range of 0.25–1 A cm^{-2} . As shown in Fig. 8e, the faradaic efficiencies of YEBCG cell were 96.5, 92.9, and 87.8% at 500, 550, and 600 °C at 0.75 A cm^{-2} . As the operation temperature increased, the faradaic efficiency of the YEBCG cell decreased because the electronic charge carrier contribution increases with temperature (Fig. S7†).^{9,11}

We evaluated the long-term durability of cells under a constant current density of 0.2 (PCFC mode) and -0.2 A cm^{-2} (PCEC mode) at 600 °C to investigate the feasibility of the swedenborgite structured YEBCG electrode materials under RPCC conditions. As shown in Fig. 8f, no degradation was observed during the entire 100 h PCFC, 100 h PCEC, and 800 h RPPC mode (cycles of PCFC for 10 h and PCEC for 10 h) operation. This result further demonstrates the effectiveness of the Er and Ga co-doped YBC electrode material for the high performance of RPCCs with excellent durability at intermediate temperatures.

Conclusions

A systematic examination to gain a fundamental understanding of YBC-based swedenborgites oxides was carried out in order to boost the ORR/OER catalytic activity and phase stability of air electrode materials used in SOFCs and RPCCs at reduced temperatures. YBC ($\text{Y}_{0.8}\text{Er}_{0.2}\text{BaCo}_{3.2}\text{Ga}_{0.8}\text{O}_{7+\delta}$) with Er- and Ga-doped into Y- and Co-sites, respectively, presented lower ASRs with a lower activation energy of 0.69 eV in a symmetric cell when compared with other doped YBC materials. Both D_{chem} and k_{chem} values of YEBCG indicated much faster processes than those in other perovskite structured materials in the intermediate temperature range. Upon doping atoms with different oxidation states and ionic radii, and high electronegativity into YBC, changes in interatomic spacings due to local lattice distortions occurred, these changes eventually lead to modifications in electronic states and covalent bonding characters of Co–O that boost the electrocatalytic activity of YEBCG. In addition, the high content of highly oxidative oxygen species on the YEBCG surface contributed to improve its OH^- adsorption kinetics and electron transport properties for ORR/OER. The YEBCG cells achieved notably high power densities of 1.30 and 1.35 W cm^{-2} for SOFCs and PCFCs, respectively, at 700 °C. In addition, the YEBCG cells reached a current density of -1.75 A cm^{-2} at 600 °C under an applied voltage of 1.4 V in PCEC mode. Furthermore, the faradaic efficiency of the YEBCG cell was measured to be 97.2% under -0.5 A cm^{-2} at 500 °C, this

clearly demonstrates that the YEBCG cell produces the correct amount of H₂ to match with theory.

Author contributions

J.-S. Shin and J.-Y. Park designed all the experiments. J.-S. Shin, K. Park, M. Saqib, and M. Jo performed the synthesis of materials for the cell components and physicochemical and electrochemical analyses. J.-S. Shin, K. Park, and M. Saqib measured the cell performances under SOFC and RPCC conditions. J.-S. Shin, M. Jo, H.-T. Lim, J. H. Kim analyzed the crystalline and electronic structures of the materials. H. Park and J. Kim carried out the DFT calculation. J.-S. Shin, H.-T. Lim, J. H. Kim, and J. Kim wrote the paper. All authors contributed to writing and editing the document.

Conflicts of interest

The authors declare no conflict of interest.

Acknowledgements

This research was supported by the Mid-career Researcher and Next-generation Engineering Researchers Development Program through the National Research Foundation of Korea (NRF-2017R1A2A2A05069812 and NRF-2019H1D8A2106002) and by the Industrial Technology Innovation R&D Program of the Korea Institute of Energy Technology Evaluation and Planning (KETEP), which has been granted financial resources from the Ministry of Trade, Industry & Energy, Republic of Korea (No. 20173010032290).

References

- 1 E. P. Murray, T. Tsai and S. A. Barnett, *Nature*, 1999, **400**, 649.
- 2 K. Bae, H. S. Noh, D. Y. Jang, J. Hong, H. Kim, K. J. Yoon, J. H. Lee, B. K. Kim, J. H. Shim and J. W. Son, *J. Mater. Chem. A*, 2016, **4**, 6395.
- 3 Y. Choi, S. K. Cha, H. Ha, S. Lee, H. K. Seo, J. Y. Lee, H. Y. Kim, S. O. Kim and W. Jung, *Nat. Nanotechnol.*, 2019, **14**, 245.
- 4 Y. D. Kim, J. Yang, J. I. Lee, M. Saqib, J. S. Shin, K. Park, M. Jo, S. J. Song and J. Y. Park, *J. Power Sources*, 2020, **452**, 227758.
- 5 Y. J. Meng, X. Y. Wang, W. Zhang, C. Xia, Y. N. Liu, M. H. Yuan, B. Zhu and Y. Ji, *J. Power Sources*, 2019, **421**, 33.
- 6 W. P. Sun, M. F. Liu and W. Liu, *Adv. Energy Mater.*, 2013, **3**, 1041.
- 7 E. Fabbri, L. Bi, D. Pergolesi and E. Traversa, *Adv. Mater.*, 2012, **24**, 195.
- 8 C. C. Duan, R. J. Kee, H. Y. Zhu, C. Karakaya, Y. C. Chen, S. Ricote, A. Jarry, E. J. Crumlin, D. Hook, R. Braun, N. P. Sullivan and R. O'Hayre, *Nature*, 2018, **557**, 217.
- 9 S. Choi, C. J. Kucharczyk, Y. G. Liang, X. H. Zhang, I. Takeuchi, H. I. Ji and S. M. Haile, *Nat. Energy*, 2018, **3**, 202.
- 10 M. Saqib, J. I. Lee, J. S. Shin, K. Park, Y. D. Kim, K. B. Kim, J. H. Kim, H. T. Lim and J. Y. Park, *J. Electrochem. Soc.*, 2019, **166**, F746.
- 11 C. C. Duan, R. Kee, H. Y. Zhu, N. Sullivan, L. Z. Zhu, L. Z. Bian, D. Jennings and R. O'Hayre, *Nat. Energy*, 2019, **4**, 230.
- 12 Y. Zhang, R. Knibbe, J. Sunarso, Y. J. Zhong, W. Zhou, Z. P. Shao and Z. H. Zhu, *Adv. Mater.*, 2017, **29**, 1700132.
- 13 E. D. Wachsman and K. T. Lee, *Science*, 2011, **334**, 935.
- 14 C. C. Duan, D. Hook, Y. C. Chen, J. H. Tong and R. O'Hayre, *Energy Environ. Sci.*, 2017, **10**, 176.
- 15 Y. Chen, S. Yoo, K. Pei, D. C. Chen, L. Zhang, B. deGlee, R. Murphy, B. T. Zhao, Y. X. Zhang, Y. Chen and M. L. Liu, *Adv. Funct. Mater.*, 2018, **28**, 2458.
- 16 D. Ding, X. X. Li, S. Y. Lai, K. Gerdes and M. L. Liu, *Energy Environ. Sci.*, 2014, **7**, 552.
- 17 K. Y. Park, Y. D. Kim, J. I. Lee, M. Saqib, J. S. Shin, Y. Seo, J. H. Kim, H. T. Lim and J. Y. Park, *ACS Appl. Mater. Interfaces*, 2019, **11**, 457.
- 18 S. Park, S. Choi, J. Shin and G. Kim, *RSC Adv.*, 2014, **4**, 1775.
- 19 J. Kim, S. Sengodan, G. Kwon, D. Ding, J. Shin, M. L. Liu and G. Kim, *ChemSusChem*, 2014, **7**, 2811.
- 20 R. Zohourian, R. Merkle, G. Raimondi and J. Maier, *Adv. Funct. Mater.*, 2018, **28**, 1801241.
- 21 F. Briec, G. Dezanneau, M. Hayoun and H. Dammak, *Solid State Ionics*, 2017, **309**, 187.
- 22 L. Li, F. J. Jin, Y. Shen and T. M. He, *Electrochim. Acta*, 2015, **182**, 682.
- 23 A. S. Harvey, F. J. Litterst, Z. Yang, J. L. M. Rupp, A. Infortuna and L. J. Gauckler, *Phys. Chem. Chem. Phys.*, 2009, **11**, 3090.
- 24 K. Świerczek, K. Zheng and A. Klimkiewicz, *ECS Trans.*, 2013, **57**, 1993.
- 25 L. M. Zhang, S. Y. Yang, S. Z. Zhang and Y. X. Yang, *Int. J. Hydrogen Energy*, 2019, **44**, 27921.
- 26 S. Y. Istomin, O. A. Tyablikov, S. M. Kazakov, E. V. Antipov, A. I. Kurbakov, A. A. Tsirlin, N. Hollmann, Y. Y. Chin, H. J. Lin, C. T. Chen, A. Tanaka, L. H. Tjeng and Z. Hu, *Dalton Trans.*, 2015, **44**, 10708.
- 27 R. Pelosato, G. Cordaro, D. Stucchi, C. Cristiani and G. Dotelli, *J. Power Sources*, 2015, **298**, 46.
- 28 J. H. Kim, Y. N. Kim, S. M. Cho, H. Wang and A. Manthiram, *Electrochim. Acta*, 2010, **55**, 5312.
- 29 D. Medvedev, J. Lyagaeva, G. Vdovin, S. Beresnev, A. Demin and P. Tsiakaras, *Electrochim. Acta*, 2016, **210**, 681.
- 30 M. A. Bhat, R. A. Zargar, A. Modi, M. Arora and N. K. Gaur, *Mater. Sci.*, 2016, **34**, 786.
- 31 G. K. Tian, H. Chen, C. X. Lu, Y. Xin, Q. Li, J. A. Anderson and Z. L. Zhang, *Catal. Sci. Technol.*, 2016, **6**, 4511.
- 32 N. Hollmann, Z. Hu, M. Valldor, A. Maignan, A. Tanaka, H. H. Hsieh, H. J. Lin, C. T. Chen and L. H. Tjeng, *Phys. Rev. B: Condens. Matter Mater. Phys.*, 2009, **80**, 085111.
- 33 A. Maignan, S. Hebert, V. Caignaert, V. Pralong and D. Pelloquin, *Solid State Commun.*, 2008, **147**, 470.
- 34 D. S. Tsvetkov, V. Pralong, N. S. Tsvetkova and A. Y. Zuev, *Solid State Ionics*, 2015, **278**, 1.
- 35 K. Y. Lai and A. Manthiram, *Chem. Mater.*, 2016, **28**, 9077.
- 36 N. A. Danilov, A. P. Tarutin, J. G. Lyagaeva, E. Y. Pikalova, A. A. Murashkina, D. A. Medvedev, M. V. Patrakeev and A. K. Demin, *Ceram. Int.*, 2017, **43**, 15418.

- 37 D. K. Lim, S. Y. Jeon, B. Singh, J. Y. Park and S. J. Song, *J. Alloys Compd.*, 2014, **610**, 301.
- 38 I. Yasuda and T. Hikita, *J. Electrochem. Soc.*, 1994, **141**, 1268.
- 39 F. Ciucci, *Solid State Ionics*, 2013, **239**, 28.
- 40 G. Kresse and J. Furthmüller, *Comput. Mater. Sci.*, 1996, **6**, 15.
- 41 P. E. Blöchl, *Phys. Rev. B: Condens. Matter Mater. Phys.*, 1994, **50**, 17953.
- 42 J. P. Perdew, K. Burke and M. Ernzerhof, *Phys. Rev. Lett.*, 1996, **77**, 3865.
- 43 V. I. Anisimov, F. Aryasetiawan and A. I. Lichtenstein, *J. Phys.: Condens. Matter*, 1997, **9**, 767.
- 44 D.-H. Seo, H. Gwon, S.-W. Kim, J. Kim and K. Kang, *Chem. Mater.*, 2010, **22**, 518.
- 45 B. Sabir, G. Murtaza and R. M. A. Khalil, *J. Mol. Graphics Modell.*, 2020, **94**, 107482.
- 46 A. Jain, G. Hautier, S. P. Ong, C. J. Moore, C. C. Fischer, K. A. Persson and G. Ceder, *Phys. Rev. B: Condens. Matter Mater. Phys.*, 2011, **84**, 045115.
- 47 B. J. Morgan, D. O. Scanlon and G. W. Watson, *J. Mater. Chem.*, 2009, **19**, 5175.
- 48 W. Wong-Ng, W. Xie, Y. Yan, G. Liu, J. Kaduk, E. Thomas and T. Tritt, *J. Appl. Phys.*, 2011, **110**, 113706.
- 49 A. Gomez, D. Fuchs and O. Moran, *Thin Solid Films*, 2013, **545**, 140.
- 50 L. M. Hou, Q. B. Yu, K. Wang, T. Wang, F. Yang and S. Zhang, *J. Therm. Anal. Calorim.*, 2019, **137**, 317.
- 51 M. Iakovleva, S. Zimmermann, J. Zeisner, A. Alfonsov, H. J. Grafe, M. Valldor, E. Vavilova, B. Buchner and V. Kataev, *Phys. Rev. B*, 2017, **96**, 064417.
- 52 B. Raveau, V. Caignaert, V. Pralong and A. Maignan, *Z. Anorg. Allg. Chem.*, 2009, **635**, 1869.
- 53 O. Parkkima and M. Karppinen, *Eur. J. Inorg. Chem.*, 2014, **2014**, 4056.
- 54 X. F. Ding, Z. P. Gao, D. Ding, X. Y. Zhao, H. Y. Hou, S. H. Zhang and G. L. Yuan, *Appl. Catal., B*, 2019, **243**, 546.
- 55 J. Suntivich, H. A. Gasteiger, N. Yabuuchi, H. Nakanishi, J. B. Goodenough and Y. Shao-Horn, *Nat. Chem.*, 2011, **3**, 647.
- 56 J. Park, M. Risch, G. Nam, M. Park, T. J. Shin, S. Park, M. G. Kim, Y. Shao-Horn and J. Cho, *Energy Environ. Sci.*, 2017, **10**, 129.
- 57 T. Hong, K. S. Brinkman and C. R. Xia, *ChemElectroChem*, 2016, **3**, 805.
- 58 W. He, X. L. Wu, G. M. Yang, H. G. Shi, F. F. Dong and M. Ni, *ACS Energy Lett.*, 2017, **2**, 301.
- 59 P. Z. Li, Z. H. Wang, X. Q. Huang, L. Zhu, Z. Q. Cao, Y. H. Zhang, B. Wei, X. B. Zhu and Z. Lu, *J. Alloys Compd.*, 2017, **705**, 105.
- 60 J. Wang, M. Saccoccio, D. J. Chen, Y. Gao, C. Chen and F. Ciucci, *J. Power Sources*, 2015, **297**, 511.
- 61 Y. L. Zhu, W. Zhou, R. Ran, Y. B. Chen, Z. P. Shao and M. L. Liu, *Nano Lett.*, 2016, **16**, 512.
- 62 D. Rupasov, T. Makarenko and A. J. Jacobson, *Solid State Ionics*, 2014, **265**, 68.
- 63 P. F. Haworth, S. Smart, J. M. Serra and J. C. D. da Costa, *Phys. Chem. Chem. Phys.*, 2012, **14**, 9104.
- 64 Y. B. Chen, B. M. Qian and Z. P. Shao, *J. Power Sources*, 2015, **294**, 339.
- 65 Y. Lu, H. L. Zhao, X. W. Chang, X. F. Du, K. Li, Y. H. Ma, S. Yi, Z. H. Du, K. Zheng and K. Swierczek, *J. Mater. Chem. A*, 2016, **4**, 10454.
- 66 D. J. Chen and Z. P. Shao, *Int. J. Hydrogen Energy*, 2011, **36**, 6948.
- 67 S. X. She, Y. L. Zhu, Y. B. Chen, Q. Lu, W. Zhou and Z. P. Shao, *Adv. Energy Mater.*, 2019, **9**, 1970071.
- 68 J. Dai, Y. L. Zhu, Y. C. Yin, H. A. Tahini, D. Q. Guan, F. F. Dong, Q. Lu, S. C. Smith, X. W. Zhang, H. T. Wang, W. Zhou and Z. P. Shao, *Small*, 2019, **15**, 1903120.
- 69 W. T. Hong, K. A. Stoerzinger, Y.-L. Lee, L. Giordano, A. Grimaud, A. M. Johnson, J. Hwang, E. J. Crumlin, W. Yang and Y. Shao-Horn, *Energy Environ. Sci.*, 2017, **10**, 2190.
- 70 J. Hwang, R. R. Rao, L. Giordano, Y. Katayama, Y. Yu and Y. Shao-Horn, *Science*, 2017, **358**, 751.
- 71 Q. Xu, D. P. Huang, F. Zhang, W. Chen, M. Chen and H. X. Liu, *J. Alloys Compd.*, 2008, **454**, 460.